



RESEARCH ARTICLE

10.1029/2021JD035548

What Contributes to the Inter-Annual Variability in Tropical Lower Stratospheric Temperatures?

Alison Ming¹  and Peter Hitchcock² 

¹Department of Applied Mathematics and Theoretical Physics, University of Cambridge, Cambridge, UK, ²Cornell University, Ithaca, NY, USA

Key Points:

- Inter-annual variability in lower tropical stratospheric temperatures has been reconstructed
- Ozone and dynamical heating dominate. Aerosol and water vapor contributions are not negligible
- Ozone associated with the Quasi-biennial oscillation contributes substantially, particularly during the 2016 disruption

Supporting Information:

Supporting Information may be found in the online version of this article.

Correspondence to:

A. Ming,
A.Ming@damtp.cam.ac.uk

Citation:

Ming, A., & Hitchcock, P. (2022). What contributes to the inter-annual variability in tropical lower stratospheric temperatures? *Journal of Geophysical Research: Atmospheres*, 127, e2021JD035548. <https://doi.org/10.1029/2021JD035548>

Received 9 JUL 2021
Accepted 14 DEC 2021

Author Contributions:

Conceptualization: Alison Ming
Formal analysis: Alison Ming
Funding acquisition: Alison Ming
Investigation: Alison Ming
Methodology: Alison Ming, Peter Hitchcock
Project Administration: Alison Ming
Resources: Alison Ming
Software: Alison Ming
Supervision: Peter Hitchcock
Validation: Alison Ming
Visualization: Alison Ming
Writing – original draft: Alison Ming, Peter Hitchcock
Writing – review & editing: Alison Ming, Peter Hitchcock

© 2021 The Authors.

This is an open access article under the terms of the [Creative Commons Attribution-NonCommercial License](https://creativecommons.org/licenses/by/4.0/), which permits use, distribution and reproduction in any medium, provided the original work is properly cited and is not used for commercial purposes.

Abstract The inter-annual variability in mid and lower stratospheric temperatures for the period 1984–2019 is decomposed into dynamical and radiative contributions using a radiative calculation perturbed with changes in dynamical heating, trace gases and aerosol optical depth. The temperature timeseries obtained is highly correlated with the de-seasonalized ERA5 temperature ($r^2 > 0.6$ in the region 15 to 70 hPa, 1992 to 2019—after the Pinatubo volcanic eruption). Ozone and dynamical heating contributions are found to be equally important, with water vapor, stratospheric aerosols, and carbon dioxide playing smaller roles. Prominent aspects of the temperature timeseries are closely reproduced, including the 1991 Pinatubo volcanic eruption, the year-2000 water vapor drop, and the 2016 Quasi-biennial oscillation (QBO) disruption. Below 20 hPa, ozone is primarily controlled by transport and is positively correlated to the upwelling. This ozone-transport feedback acts to increase the temperature response to a change in upwelling by providing an additional ozone-induced radiative temperature change. This can be quantified as an enhancement of the dynamical heating of about 20% at 70 hPa. A Principal Oscillation Pattern (POP) analysis is used to estimate the contribution of the ozone QBO (± 1 K at 70 hPa). The non-QBO ozone variability is also shown to be significant. Using the QBO leading POP timeseries as representative of the regular QBO signal, the QBO 2016 disruption is shown to have an anomalously large radiative impact on temperature due to the ozone change (>3 K at 70 hPa).

Plain Language Summary Temperatures in the lower stratosphere vary substantially from year to year and play a major role in determining the composition of the stratosphere, which in turn plays an important role in Earth’s energy budget. Understanding this variability is thus key to understanding the properties of the stratosphere. We calculate the amount of heating due to changes in four main factors (circulation, ozone, water vapor, and aerosol). This allows us to decompose the observed temperature changes into these main factors with good agreement during the time period studied (1984–2019). Our method also allows us to analyze anomalously large temperature changes such as those during volcanic eruptions and the recent disruption in the Quasi-biennial oscillation. We find that ozone changes play a key role throughout the time period analyzed. Our findings indicate that temperature changes related to composition (particularly ozone) are critical in determining the variability of temperatures in the lower tropical stratosphere. They highlight the need to validate these processes in global models.

1. Introduction

The inter-annual variability of temperatures in the tropical lower stratosphere is of interest since temperature in this region controls the entry of water vapor into the stratosphere which can then modify the surface radiative balance (Fueglistaler et al., 2014). The chemical composition of the stratosphere is strongly impacted by the balance reached between the circulation, radiation and chemistry in this region. A number of trace species including ozone, water vapor, and stratospheric aerosols in this region have significant climate impacts. Temperatures in the tropical lower stratosphere are closely coupled to these trace species and thus to their influence on the energy balance of the climate system. Despite their importance, temperatures in this region exhibit more uncertainty in reanalysis datasets than in any other region in the atmosphere below 10 hPa (see Hersbach et al., 2020, their Figure 11). A detailed understanding of the processes that determine temperatures in this region is thus desirable.

The inter-annual variability in dynamical heating arising from changes in upwelling in the Brewer-Dobson circulation has been identified as a main contributor to this temperature variability (Fueglistaler et al., 2014). An increase in upwelling decreases temperature below radiative equilibrium by adiabatic cooling. It also changes the transport of ozone, water vapor and aerosol—all radiatively active trace species. These species induce local and

non-local changes to the radiative balance. Several studies have focused on this interaction in the tropical lower stratosphere, in the time mean and for the seasonal cycle (Charlesworth et al., 2019; Forster et al., 1997; Ming et al., 2017). These studies make use of single column radiative calculations, typically assuming that the dynamical heating is fixed, and have proved to be instrumental in understanding the contribution of radiative transfer to temperature variability in this region.

This work builds on previous such studies but focuses on quantifying the different contributions of the dynamical heating and the radiative heating to the temperature inter-annual variability. As observation systems and reanalysis models have improved, the temperature variability in the tropical lower stratosphere has become better constrained with good agreement between the modern reanalysis datasets (ERA-Interim, JRA-55, MERRA-2, and CFSR) and radio occultation measurements particularly after the year 2000 (Tegtmeier et al., 2020). Since temperature is well constrained and dynamically linked to upwelling and radiatively linked to changes in trace species, understanding the temperature variability is particularly relevant to elucidating the properties of the Tropical Tropopause Layer (TTL) (Fueglistaler et al., 2014).

In this study, we test the importance of large scale upwelling and trace gas changes to temperature variability using a single column clear-sky radiative calculation that is continuously perturbed. We show that we can successfully reconstruct the time series of inter-annual variability and quantify the contributions of the various perturbations. We demonstrate that ozone changes are of similar importance to dynamical variability on inter-annual timescales, extending results from previous studies that emphasized the role of ozone in determining the time-mean structure of the TTL (Charlesworth et al., 2019; Thuburn & Craig, 2002) and the large seasonal cycle in TTL temperatures (Chae & Sherwood, 2007; Fueglistaler et al., 2011; Gilford & Solomon, 2017; Ming et al., 2017).

A significant part of the ozone variability is driven by the Quasi-biennial oscillation (QBO) which dominates the variability of the tropical stratosphere. The QBO is characterized by descending bands of zonal winds, alternating between eastward and westward. Eastward (vertical) shear is associated with anomalously warm temperatures, while westward shear is associated with anomalously cold temperatures, consistent with thermal wind balance. These are further associated with a secondary meridional circulation (Plumb & Bell, 1982), with relative ascent in eastward shear zones and descent in westward shear zones. Below about 20 hPa, photo-chemical lifetimes of ozone are long and transport dominates the ozone budget (see e.g., Nagashima et al., 1998). Increased downwelling leads to higher ozone mixing ratios. Hence there is a large component of QBO variability in ozone (Pahlavan et al., 2021). We find that although a large part of the ozone variability is indeed related to the QBO, a large non-QBO component is also present. Both contribute substantially to inter-annual variability in temperatures.

Another important contribution arises from explosive volcanic eruptions that emit aerosol into the stratosphere. This aerosol warms the lower stratosphere (Robock, 2000). During the time period we analyze, the Pinatubo volcanic eruption in 1991, in the tropics, is the largest contributor, although the effects of smaller eruptions are also noted. By including a simple representation of the eruptions using the observed aerosol optical depth, we are able to reproduce the observed temperature signal following the Pinatubo volcanic eruption.

The other contributions to temperature come from water vapor variations which are modulated by temperatures at the cold point and from the increase in carbon dioxide in the atmosphere.

The calculations in this work make a clear sky assumption and do not explicitly simulate dynamics or transport. Instead we impose distributions of trace species from observations and adiabatic heating inferred from upwelling taken from the ERA5 reanalysis. The calculations do not explicitly model potential feedbacks between these drivers, such as transport effects or meridional circulations driven by diabatic heating. Nonetheless our calculation does provide insight into these interactions. We find that the ozone change amplifies the temperature response to the dynamical heating. Increases in upwelling are correlated to decreases in ozone (e.g., Randel et al., 2007). Both of these changes lead to a decrease in temperature. This positive feedback of ozone onto temperatures can be described as an increase in radiative timescales or as an increase in the effective dynamical heating and we present estimates of these quantities.

The paper is organized as follows. Section 2 describes the methodology that extends single column radiative calculations to inter-annually varying perturbations. Section 3 describes the data and radiative code. We discuss the contributions of various perturbations to temperature in Section 4 and quantify the QBO contribution in Section 5. The QBO 2016 disruption is studied in more detail in Section 5.1. Section 6 focuses on the modification of radi-

ative damping resulting from ozone. Finally, in Section 7, we discuss and summarize our results. The appendix contains details of the correlation between our radiative calculation and ERA5 temperatures (Appendix A), further details of the carbon dioxide linear trend on temperature (Appendix B) and a brief summary of the POP analysis (Appendix C). We also provide a Supporting Information S1 file that contains additional plots of relevance.

2. Inter-Annually Evolving Fixed Dynamical Heating

Consider the thermodynamic equation in the Transformed Eulerian Mean framework (Andrews et al., 1987), neglecting eddy terms which are small,

$$\partial_t \bar{T} = \bar{Q}_{\text{rad}} - \bar{w}^* \bar{S} - \bar{v}^* \partial_y \bar{T} = \bar{Q}_{\text{rad}}(\bar{\chi}, \bar{T}) + \bar{Q}_{\text{dyn}}, \quad (1)$$

which predicts the rate of change of zonal mean temperature, \bar{T} , with time, t where $\bar{(\cdot)}$ represents a zonal mean. The dynamical heating, \bar{Q}_{dyn} , is defined by the second equality in Equation 1. \bar{v}^* and \bar{w}^* are the horizontal and vertical components of the mean residual velocity respectively. We calculated the inter-annual variability in the meridional advection term of the dynamical heating (not shown) and found it to be small. Hence it is neglected in this work. y is the meridional coordinate. $\bar{S} = \partial_z \bar{T} + \kappa \bar{T} / H$ is a measure of the static stability where z is the log-pressure height. $z = -H \log(\sigma)$ where H is a scale height taken to be 7 km and $\sigma = p/p_0$ where p is pressure and $p_0 = 1,000$ hPa. $\kappa = R/c_p \approx 2/7$ where R is the gas constant for dry air and c_p is the specific heat at constant pressure. The radiative heating, \bar{Q}_{rad} , depends, in general, on temperature, \bar{T} , and the distributions of various radiatively active components, $\bar{\chi}$, including clouds, aerosols and trace gases.

A common method for estimating the temperature change resulting from a perturbation in trace gas is the Fixed Dynamical Heating (FDH) calculation. The FDH calculation assumes that for a given perturbation, the dynamical heating remains the same as the unperturbed state, allowing the new temperature required to reach radiative equilibrium to be calculated. This method was modified by Forster et al. (1997) to study seasonally evolving forcings by allowing the dynamical heating to evolve with time and iterating to a new seasonal cycle in temperatures. This method is called the seasonally evolving fixed dynamical heating (SEFDH) calculation and has provided insight into radiative processes at play in the tropical lower stratosphere on seasonal timescales. We further modify this calculation and introduce the inter-annually evolving fixed dynamical heating calculation (IEFDH) as method of estimating the contributions of inter-annually varying changes in trace gas concentrations on temperatures.

The unperturbed state of the stratosphere is defined as the state in which the radiative heating is balanced by dynamical heating:

$$\bar{Q}_{\text{rad}}^\circ = \bar{Q}_{\text{rad}}(\bar{\chi}^0, \bar{T}^0) = -\bar{Q}_{\text{dyn}}^\circ, \quad (2)$$

where $(\cdot)^\circ$ denotes the unperturbed state. The radiative heating in the unperturbed state, $\bar{Q}_{\text{rad}}^\circ$, is calculated using the time mean values of temperature, \bar{T}^0 , and mixing ratios of trace species, $\bar{\chi}^0$. Equation 2 is then used to calculate the time mean $\bar{Q}_{\text{dyn}}^\circ$.

The system is now perturbed by imposing the inter-annual variation in a trace species in the stratosphere. The trace species are represented by $\bar{\chi}$ and include ozone (O_3), water vapor (H_2O), carbon dioxide (CO_2) and aerosols. Note that we apply perturbations individually. For example, ozone is allowed to vary whilst all other trace species are held at their time mean values. Temperature, \bar{T} , evolves forward as

$$\partial_t \bar{T} = \bar{Q}_{\text{rad}}(\bar{\chi}, \bar{T}) + \bar{Q}_{\text{dyn}}^\circ, \quad (3)$$

where we assume that the dynamical heating does not change $\bar{Q}_{\text{dyn}}^\circ = -\bar{Q}_{\text{rad}}^\circ$.

Temperature changes that are used to update temperature at each time step as calculated using:

$$\partial_t \Delta \bar{T} = \bar{Q}_{\text{rad}}(\bar{\chi}, \bar{T}) - \bar{Q}_{\text{rad}}(\bar{\chi}^0, \bar{T}^0), \quad (4)$$

This method is called the IEFDH calculation. Note that unlike the FDH and SEFDH methods, the IEFDH calculation does not reach equilibrium as the system is continuously being perturbed.

Finally, following a similar method to Ming et al. (2017), we estimate the temperature changes associated with the upwelling by modifying the IEFDH calculation and allowing the dynamical heating to vary. We calculate the inter-annual variation in dynamical heating, $\Delta\bar{Q}_{\text{dyn}}$, using ERA5 data as $-\bar{w}^* \bar{S}$ and impose this as a perturbation whilst keeping trace gas concentrations, $\bar{\chi}^0$, fixed. Temperatures follow:

$$\partial_t \bar{T} = \bar{Q}_{\text{rad}}(\bar{\chi}^0, \bar{T}) - \bar{w}^* \bar{S} \quad (5)$$

3. Data and Methods

Ozone and water vapor mixing ratios are obtained from the Stratospheric Water and OzOne Satellite Homogenized (SWOOSH) data set (Davis et al., 2016; Tummon et al., 2015) which is formed from a combination of measurements from five limb and solar occultation satellites from 1984 to 2015, namely: SAGE-II/III, UARS HALOE, UARS MLS, and Aura MLS instruments. We use the anomaly filled time series from SWOOSH. Values below 316 hPa are obtained by linear interpolation to the surface values from the ERA5 data set. The results in this paper are not sensitive to this choice of method for in-filling tropospheric data. This was tested by perturbing tropospheric profiles within reasonable bounds and noting that the effect on the results presented here was negligible. Stratospheric aerosol optical depth at 525 nm is obtained from GloSSAC v2.0 (Kovilakam et al., 2020; NASA/LARC/SD/ASDC, 2018). The trace gas data and stratospheric aerosol optical depth data are retrieved as monthly data which is then linearly interpolated to daily data. The inter-annual variations in ozone and water vapor are plotted in Figures S1 and S2 of Supporting Information S1 respectively.

Temperature and wind data are taken from the ERA-5 reanalysis data set covering the period 1984 to 2019 (with ERA 5.1 for the period 2000 to 2006) (C3S, 2017; Hersbach et al., 2020), using data retrieved at a horizontal resolution of 1°, at 3-hourly analysis time intervals and on 137 model levels. Transformed Eulerian Mean residual velocities are calculated on the original retrieved data before being interpolated to the grids used in the radiative calculations described below. We first use the Eulerian meridional velocity and temperature to calculate the mean residual horizontal velocity. This quantity is then used to calculate the residual streamfunction and the mean residual vertical velocity. Since we are focusing on the inter-annual variability, the data is smoothed by computing monthly averages and then linearly interpolating to daily values. Trends in the various quantities are not removed except where explicitly stated.

The radiative calculations use the Morcrette (1991) broad-band radiation scheme, which includes updates to the longwave absorption properties of water vapor (Zhong & Haigh, 1995). The longwave part of the code has eight bands in the thermal infrared: 0–350 cm⁻¹ and 1,450–1,880 cm⁻¹ combined band, 350–500 cm⁻¹, 500–800 cm⁻¹, 800–970 cm⁻¹, 970–1,110 cm⁻¹, 1,110–1,250 cm⁻¹, 1,250–1,450 cm⁻¹, and 1,880–3,000 cm⁻¹. The shortwave scheme uses two bands and includes the effects of water vapor, ozone and uniformly mixed gases. Solar insolation is calculated at each latitude and the shortwave heating rates take into account diurnal variations by using a Gaussian quadrature method with three zenith angles. The solar constant is set to 1,376 Wm⁻². All calculations use zonal mean data at 5° intervals in latitude, on 100 pressure levels and run from 1984 to 2016. Clear sky calculations are performed unless otherwise stated. The albedo is taken from ERA5 reanalysis data. Carbon dioxide is assumed to be well mixed, with a volume mixing ratio set to 345 ppmv, for all calculations except in the experiment where the linear trend in CO₂ is included. We assume that CO₂ has increased linearly from 345 ppmv (1,984 value) to 412 ppmv (2019 value) and calculate the temperature change using a simple FDH calculation. A time step of 1 day is used for all radiative calculations.

Similarly to other fixed dynamical heating calculations (Forster et al., 1997; Ming et al., 2017), we choose a level above which temperatures will be adjusted and below which temperatures will remain fixed to the time mean. We choose 130 hPa as this level for various reasons. In the context of the seasonal cycle, the same level was chosen in Ming et al. (2017) since there is a sharp decay in the amplitude of the seasonal cycle below 130 hPa. This points to a different process that keeps temperature variability low. Moreover, satellite observations show that deep convection penetrates into the lower stratosphere (see Figure 2 of Schoeberl et al., 2018) and we can argue that the response is purely radiative above 130 hPa. The effect of choosing a different level, 200 hPa (similar to Forster et al., 2007), is shown in Figure S3a in Supporting Information S1. Note that choosing 200 hPa worsens the agreement with ERA5 at all levels between 100 and 140 hPa (Figure S3 in Supporting Information S1).

All the perturbations add linearly to give the total temperature change (not shown).

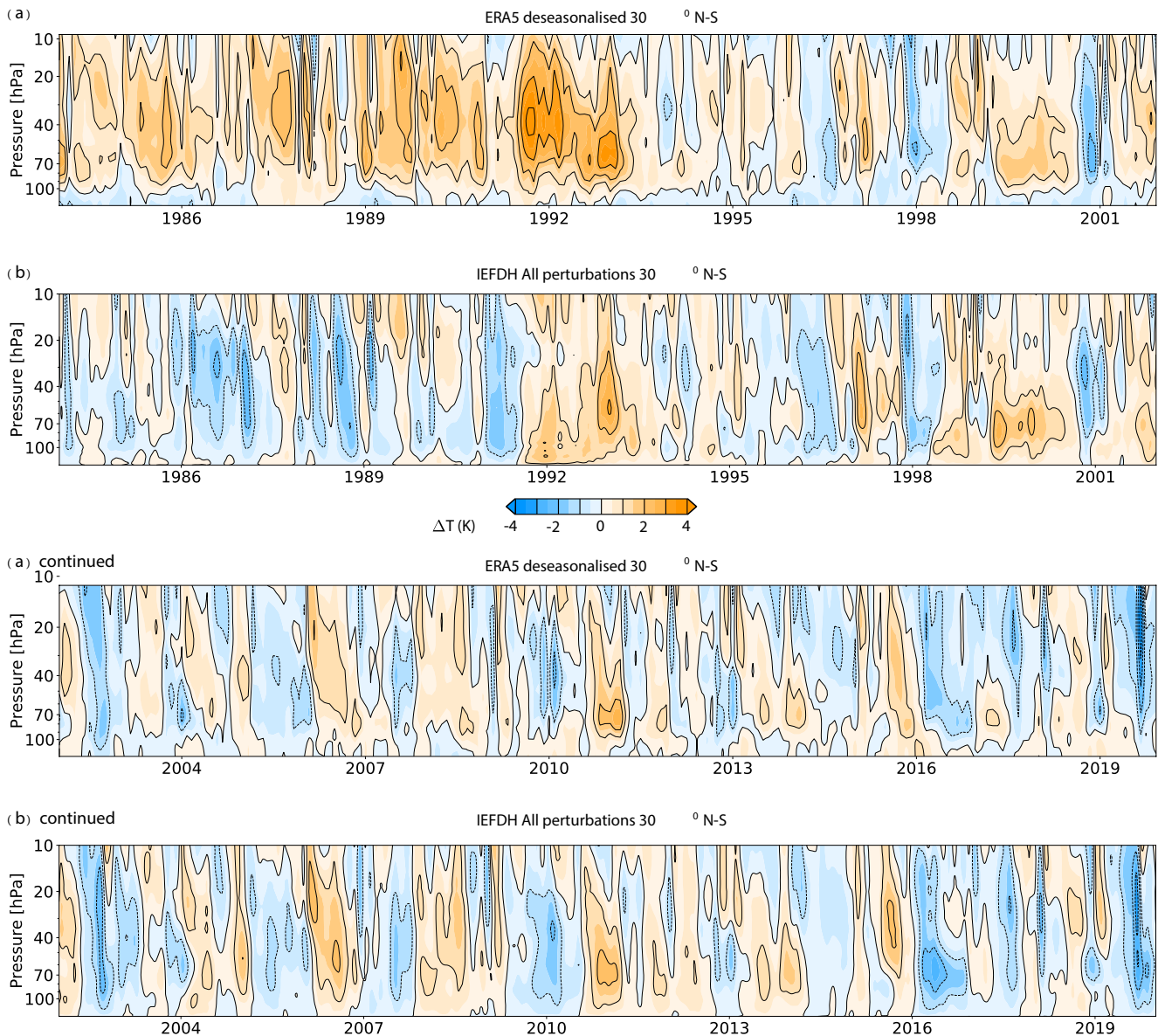


Figure 1. Inter-annual variability in temperature averaged between 30° N – S at different pressure levels from (a) ERA5 (b) the inter-annually evolving fixed dynamical heating radiative calculation with all perturbations. Differences are evaluated with respect to the reference period 2002–2010. Note that the plots are split into two panels spanning 1984 to 2001 and 2002 to 2019 for clarity. See main text for further details.

4. IEFDH Results

The temperature inter-annual variability is reconstructed using the dynamical heating perturbation taken from ERA-5, ozone, water vapor, aerosol optical depth and carbon dioxide perturbations (labeled as the “all perturbations” experiment). Figure 1 shows the ERA-5 temperature inter-annual variability averaged between 30° N – S together with the corresponding temperature time series re-constructed using the IEFDH calculation with all the perturbations listed above.

The figure shows that these perturbations together capture the inter-annual variability in temperatures in the tropical lower and mid stratosphere with broadly good agreement throughout most of the time series after 1991 ($r^2 > 0.67$ in the region 20 to 70 hPa for 1992 to 2019, see Appendix A). The mean temperature from the IEFDH calculation before 1991 is about 0.9 K lower than ERA5. This could be due to a number of factors. For instance, reanalysis datasets are known to have jumps in the data when new instruments are assimilated and a clear jump

is visible in the global mean anomalies of temperature and ozone in ERA5 before and after the Pinatubo volcanic eruption in 1991 (Hersbach et al., 2020, their figure 25). In the IEFDH calculation, the SWOOSH data set chooses SAGE II ozone as the mean reference satellite against which ozone from UARS MLS and UARS HALOE is adjusted. These satellites became operational in October 1991. Identifying the cause of this jump is beyond the scope of the present study, but if we account for this jump by applying a constant offset, we find that the inter-annual variability in ERA5 is captured by the IEFDH calculation before 1991. The difference between the ERA5 temperature and the IEFDH calculation is shown in Figure S3 in Supporting Information S1.

Next we turn to a discussion of the dominant processes that contribute to this inter-annual variability.

4.1. Dynamical Heating and Ozone

Between 1984 and 2019, temperature at 70 hPa varies by ± 2.9 K in ERA5 and by ± 2.7 K in the IEFDH all perturbation experiment as shown in Figure 2a. Figures 2b and 2c break down the temperature time series into the contributions from the different perturbations. The equivalent plot for 90 hPa can be found in Figure S5 in Supporting Information S1. A contributor is the dynamical heating perturbation (± 2.1 K) which is consistent with the findings of Fueglistaler et al. (2014, their Figure 3). However, variations in ozone generate a comparable contribution to the temperature variation throughout the time series, of up to ± 1.6 K. In the tropical lower stratosphere, an increase in ozone results in increased absorption of shortwave radiation and upwelling longwave radiation with the longwave heating dominating (about 80%). A detailed description of the radiative processes in this region can be found in the appendix of Ming et al. (2017).

During certain time periods, temperature changes due to ozone are as large as that from dynamical heating. Two examples of this are around the year 2000, roughly coinciding with a drop in water vapor (Randel et al., 2006), and during the 2015–2016 disruption of the QBO (each of these features is discussed further below). Furthermore, ozone lags behind the dynamical heating by roughly 1 month. This is expected, since increased upwelling means less dynamical heating and more upward transport of ozone poor tropospheric air from below. We quantify this ozone-transport feedback further in Section 6.

This correlation does not always hold in the time series: anomalous dynamical warming in 2006 was not accompanied by ozone effects, nor were brief periods of dynamical cooling in 1996 and 1998. The correlation between the two effects was more substantially disrupted for nearly four years following the eruption of Pinatubo in 1991.

4.2. Water Vapor

Water vapor variations in the tropical lower stratosphere are controlled by temperature variations at the cold point where excess water vapor is freeze-dried out of the upwelling air. This pattern of water vapor variation is then advected upwards in what is known as the water vapor tape-recorder signal (Mote et al., 1994). An increase in water vapor leads to increased local longwave emission which dominates over the increased local absorption of upwelling radiation leading, in turn, to a drop in temperatures (Ming et al., 2017). The inter-annual variability in water vapor produces an IEFDH temperature change of about ± 0.4 K.

A series of drops in water vapor have been observed in the time series. The most prominent drop was in the year 2000 (Randel et al., 2006) and persisted until 2005. Lower temperatures at the cold point after the year 2000 gave rise to less water vapor entering the stratosphere which in turn led to a slight radiatively induced warming at 70 hPa. Various possible changes have been identified as the cause of the drop including increases in the Brewer-Dobson circulation (Dhomse et al., 2008), a strong El Niño followed by a La Niña and a change in the QBO phase (Brinkop et al., 2016; Garfinkel et al., 2018). The radiative impact on the surface of stratospheric water vapor changes are significant and have been quantified (Gilford et al., 2016; Maycock et al., 2014).

Following the water vapor drop in 2000, temperatures in ERA5 from 2001 to 2005 (30° N – S average) are found to be 0.46 K lower than the average from 1996 to 2000 at 70 hPa. The IEFDH calculation with all the perturbations gives a corresponding temperature change of -0.46 K at 70 hPa of which -0.42 K comes from a reduction in ozone, -0.34 K from dynamical cooling while water vapor changes led to a warming of 0.26 K. The small remainder can be attributed to changes in aerosols and carbon dioxide.

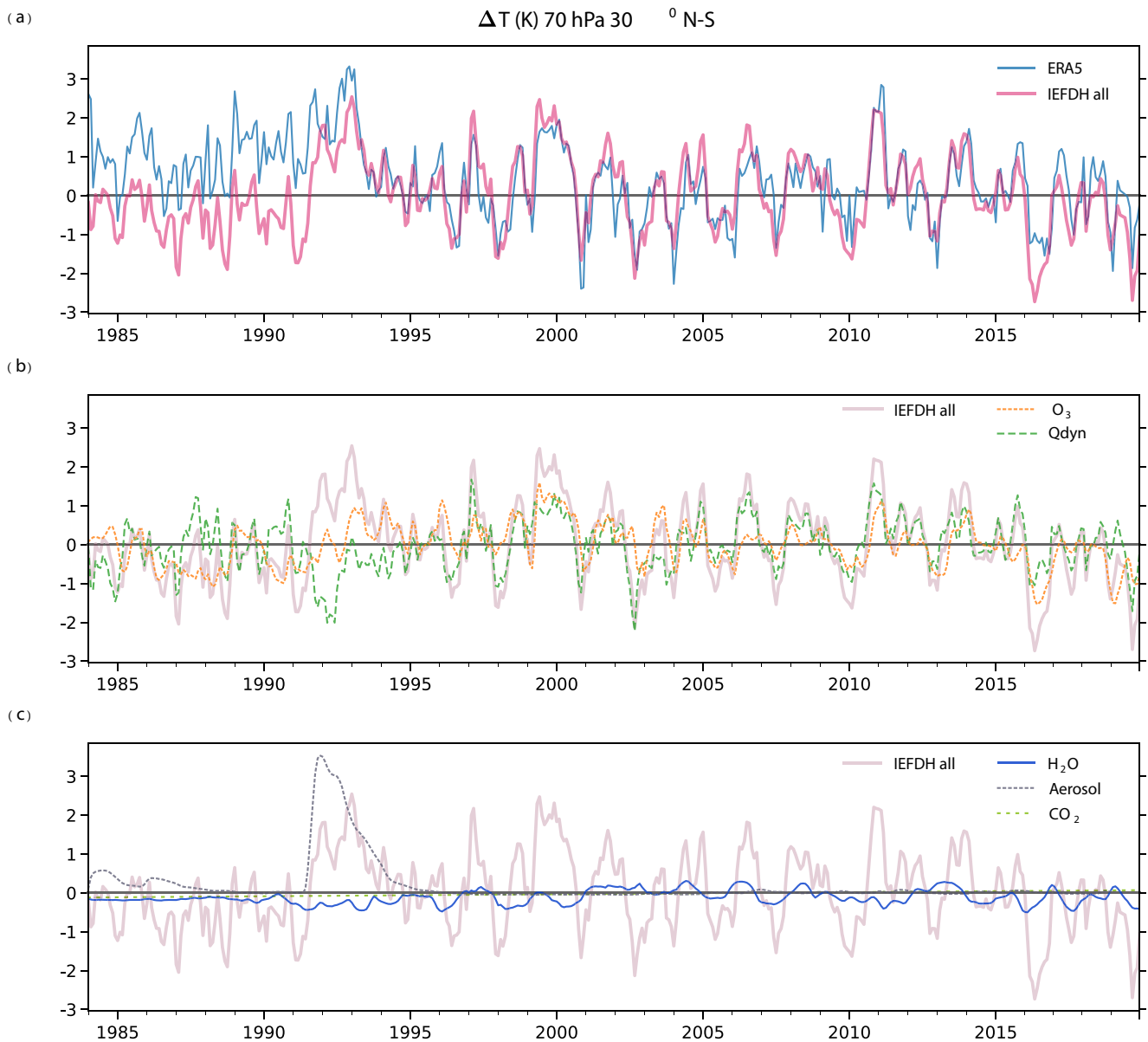


Figure 2. Inter-annual variability in temperature averaged between 30° N – S at 70 hPa, evaluated with respect to the reference period 2002–2010 for (a) ERA5 (cyan line) and the inter-annually evolving fixed dynamical heating (IEFDH) all perturbations radiative calculation (thick pink line). The individual contributions to the total are broken down into those from (b) ozone (orange dotted line) and dynamical heating (green dashed line) and (c) water vapor (blue solid line), aerosol (dotted gray line) and carbon dioxide (green dashed line). (Note that the GLOSSAC aerosol data only extends until 2018). In (b) and (c), the IEFDH all perturbations temperature change from (a) is plotted again as the thick pale pink line. See the main text for further details of the radiative calculation.

At the cold point near 90 hPa (Figure S5 in Supporting Information S1), temperatures in ERA5 changed by -0.36 K. Here again ozone dominated the signal, contributing a cooling (-0.34 K). Dynamical cooling led to a further -0.23 K change, while water vapor changes contributed a warming of 0.2 K. We note that the temperature drop in ERA5 around the year 2000 is still not large enough to explain the corresponding water vapor drop based on the Clausius-Clapeyron relationship. Fueglistaler et al. (2013) identified this as a problem in other modern reanalyses. This issue warrants further investigation but is beyond the scope of this work.

Other water vapor drops have been reported in 2011/2012 (Urban et al., 2014) and again in 2016 (Avery et al., 2017; Diallo et al., 2018). Temperatures increased during the 2011/2012 water vapor drop and decreased during the 2016 drop but in neither case were the changes as persistent as those that followed 2000 and we do not attempt to quantify the contribution from the different perturbations.

4.3. Volcanic Eruptions

Volcanic eruptions release sulphate aerosols into the tropical lower stratosphere which leads to local heating (Stenchikov et al., 1998) and increased upwelling (Poberaj et al., 2011). During the time period considered here, the largest eruption that affected temperature was the Pinatubo volcanic eruption (15°N) on June 15, 1991. The aerosol effect is represented by changing the optical depth in the IEFDH calculation. The aerosol heating leads to a maximum temperature increase of 3.3 K about 6 months after the eruption whilst the dynamical cooling produces a maximum decrease in temperature of 2 K (Figure 2c). In the 1.5 years following the eruption, there is a decrease in ozone in the region between 10° N – S arising from both dynamics and chemistry and an increase in ozone in the region polewards of 10° arising from the relative decrease in upwelling. This is consistent with the residual circulation set up as a result of the heating from the sulfate cloud. These changes in ozone are seen in modeling studies (e.g., Kilian et al., 2020; Ming et al., 2020) as well as in the SWOOSH data set (not shown). The net effect within the 30° N – S is a slight increase in ozone. As a result of the chemical and dynamical changes taking place during the eruption, the ozone and dynamical temperature changes do not appear to be correlated in the IEFDH calculation. There is a further caveat that, in the first 6 months following the eruption, a large number of ozone and water profiles below 20 hPa are filtered out of the satellite datasets due to poor retrieval quality in an opaque atmosphere. Nevertheless, the IEFDH calculation shows good agreement with the ERA5 temperature perturbation at 70 hPa in the three years following the Pinatubo eruption.

Other smaller volcanic eruptions affected temperature during this time period. The Nevado del Ruiz eruption in 1986 (Vernier et al., 2011) contributed 0.4 K at the peak and several smaller tropical eruptions after the year 2000 contribute to transient perturbations of less than 0.1 K each.

4.4. Carbon Dioxide

Carbon dioxide in the stratosphere leads to cooling. The increase in carbon dioxide concentrations adds a linear increase in temperature of 0.2 K between 1984 and 2020. This linear trend is shown in Figure 2c. The increase in temperature in the lower stratosphere is expected from an increase in CO₂ since the increased shortwave absorption dominates in the region below 40 hPa (see for e.g., Wang & Huang, 2020, for a detailed discussion). Appendix B contains more details of the vertical profile of the CO₂ induced temperature change.

5. QBO Contribution

In Figure 1, a clear downward propagating QBO pattern is visible in temperature in both plots. The contribution of the ozone changes associated with the QBO to the temperature variability will now be quantified using the IEFDH calculation. As discussed in the introduction, the secondary circulations associated with eastward and westward shear zones produce ozone anomalies. The ozone variability associated with the QBO is obtained by first identifying the Principal Oscillation Patterns (POP) (Gallagher et al., 1991; von Storch & Zwiers, 2002; Xu, 1992). A summary of the POP analysis is given in Appendix C. We choose this analysis since we are trying to resolve a propagating mode of variability and want to isolate how the spatial patterns evolve with time. We then calculate the timeseries associated with the main POP (defined by Equation C7 and shown in Figure S6 of Supporting Information S1) and take this to represent the regular QBO variability. The calculation uses a similar method to Sheshadri and Plumb (2017), who use the POP method to study the mid-latitude jet, but is applied to zonal wind and ozone with the seasonal cycle and linear trend removed. The main POP is obtained as a complex conjugate pair and similar to the linear combination of the first two empirical orthogonal functions of the respective fields.

The QBO is confined to a narrow equatorial region and we focus on the 10° N – S average in this section. Figure 3a shows the change due to the full ozone field and from the QBO at 70 hPa. The QBO variation in ozone contributes to about ± 1.0 K to the temperature variability which is consistent with previous work on this topic (Li et al., 1995). The corresponding contribution at 90 hPa is about ± 0.9 K (Figure S7 in Supporting Information S1). Figures 3b and 3c show the vertical structure of the temperature changes from the full ozone field and from the leading ozone POP timeseries respectively and Figure 3d shows the difference between (b) and (c). The QBO contributes to a larger part of the variability in ozone above 40 hPa than below. Part of this variability shown in Figure 3d will be described by other POPs (not included in this analysis) that also correspond to QBO-related variability with a slightly different timescale to the main POP. Nonetheless, there are clear periods where the

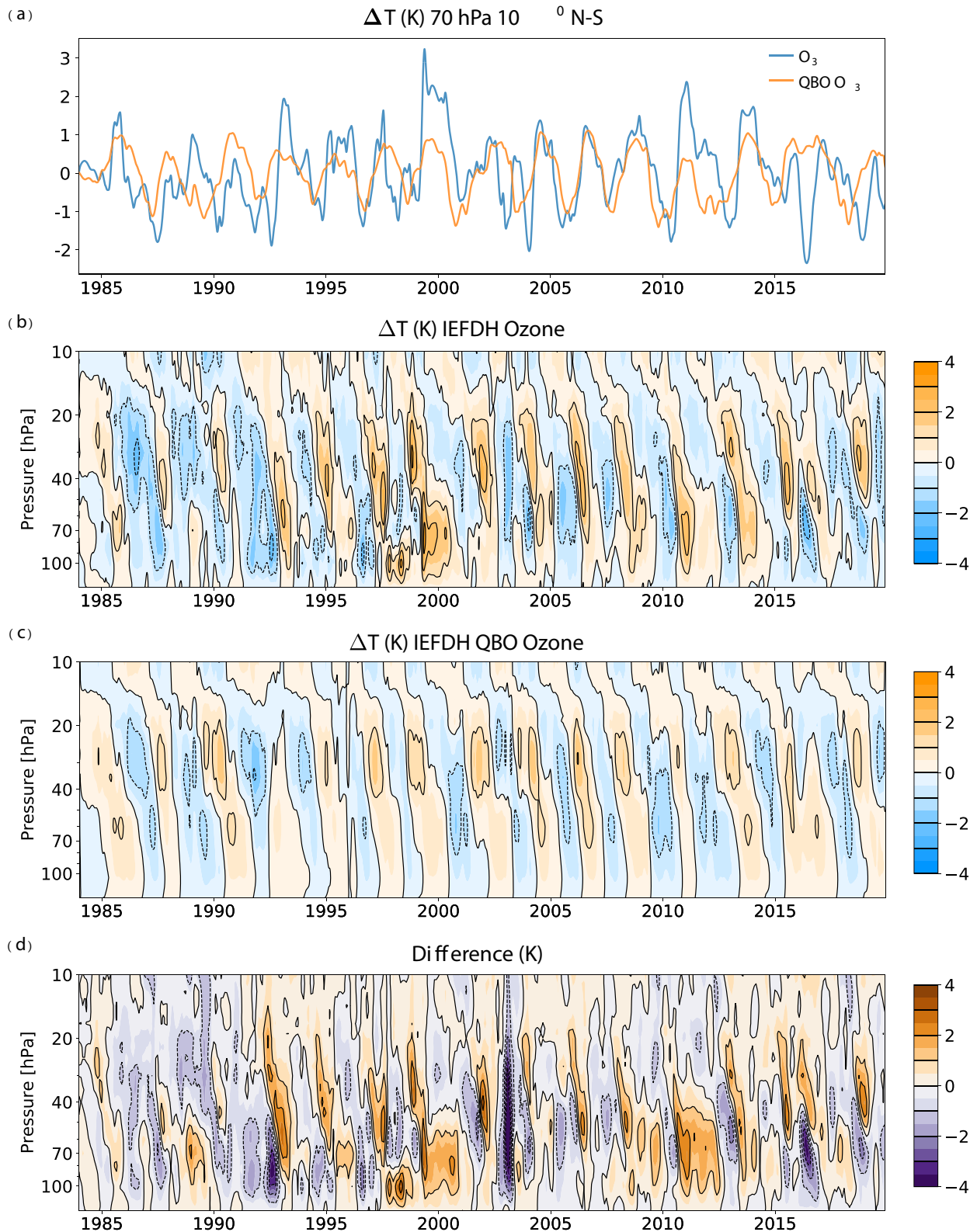


Figure 3. Inter-annually evolving fixed dynamical heating temperature change (K), averaged between 10° N – S, from inter-annual variability in ozone and from the time series associated with the leading Quasi-biennial oscillation (QBO) ozone Principal Oscillation Pattern. (a) Changes at 70 hPa. Pressure-time plots of the (b) ozone contribution (c) the QBO ozone contribution. (d) The difference between (b) and (c). Note that we are considering a narrower range of latitudes to previous plots.

behavior is not QBO-like. For instance, during the 1991 Pinatubo eruption, there is a dipole structure in the temperature change due to ozone which descends over the course of 1993. This arises from a decrease in ozone in the lower stratosphere which decreases temperature locally. The longwave radiation that is not absorbed in this region is then absorbed further up and increases temperature. During the water vapor drops in 2000 and 2010, there is a clear non-QBO ozone contribution although the two events are very different in character. There is a prolonged temperature increase due to ozone during 2000 before the water vapor drop whilst temperature increases after the water vapor drop in 2011. The 2016 water vapor drop is difficult to analyze since any ozone signal from it is obscured by the QBO 2016 disruption. This disruption event also has a descending dipole signature and will be analyzed in more detail below in Section 5.1. Finally, there is a prominent large and deep negative difference seen in 2003 which is of unknown origin.

5.1. QBO 2016 Disruption

The QBO 2016 disruption (Osprey et al., 2016) was an unusual phenomenon where a shallow westward jet formed in the eastward phase of the QBO in the lower stratosphere between 40 and 100 hPa, as can be seen in Figure 4a. The anomalous shear zones above and below this shallow westward jet are also associated with secondary circulations, similarly to the standard QBO shear zones, and give rise to large ozone anomalies. This disruption differs from the regular QBO. It is characterized by a strong jet appearing lower in the stratosphere and has a shorter vertical scale.

Ozone anomalies during this period are shown in Figure 4d and the corresponding IEFDH temperature change in Figure 4g. Using the POP analysis, we generate a timeseries corresponding to the leading POP for the zonal wind (Figure 4b) and ozone (Figure 4e). The ozone POP time series is the same as that used in the calculations above in Figure 3 (see also Figure S6 in Supporting Information S1). This can be thought of as the time series associated with the regular 28 months oscillation and will not fully capture the disruption as shown in the difference in zonal wind in Figure 4c where the shallower vertical scale of the disruption can be seen. The ozone field in the POP is also positive, corresponding to relative descent associated with the eastward shear zone that was expected to descend from the mid stratosphere during this period (Figure 4c). The ozone changes during the QBO disruption in Figure 4f are consistent with those seen by Tweedy et al. (2017), who calculate the trace gas changes as the difference from a QBO composite. The IEFDH calculation in Figure 4h shows that the regular QBO would have contributed a broad positive temperature change in the vertical with a magnitude of about 1 K around 70 hPa in the absence of a disruption. Note that although the ozone perturbations in Figure 4e maximize around 30 hPa, the temperature change due to the ozone maximizes lower down a combination of the steep vertical gradient in ozone in this region and the fact that radiative damping timescales maximize in a deep region around the cold point (Ming et al., 2017).

The effect of the QBO disruption on the ozone field is thus substantial and appears as a decrease between 40 and 100 hPa from January to June 2016 (Figure 4f). There is a corresponding decrease in temperature that extends down below the cold point with a maximum of about 3 K at 70 hPa and an increase in temperature in the region above. This is consistent with reduced local absorption of upwelling longwave radiation where ozone is low and increased absorption above the ozone perturbation. This is substantially larger than the ozone-related temperature changes associated with typical QBO variability.

Within the wider 30° N – S region, the IEFDH calculation overestimates the temperature change during the 2016 disruption compared to ERA5, by about 1.5 K (Figure 2a). We speculate that the temperature contribution from ozone is the dominant effect and that the ERA5 upwelling is poorly represented. Match and Fueglistaler (2021) reported a similar result in MERRA-2 where the large analysis tendencies recorded during the 2016 disruption reduce the confidence in the resolved momentum budget. Note that there is also a stronger downward trend in the calculated IEFDH temperatures compared to ERA5 from 2016 onward which complicates this analysis.

The QBO 2016 disruption provides an interesting case study to test the robustness of QBO-related processes in global models. The temperature change resulting from the ozone perturbations will depend strongly on correctly simulating the radiative changes and the secondary meridional circulation. It is not guaranteed that a model that captures the main zonal wind disruption will capture the details of the processes that lead to the corresponding ozone changes.

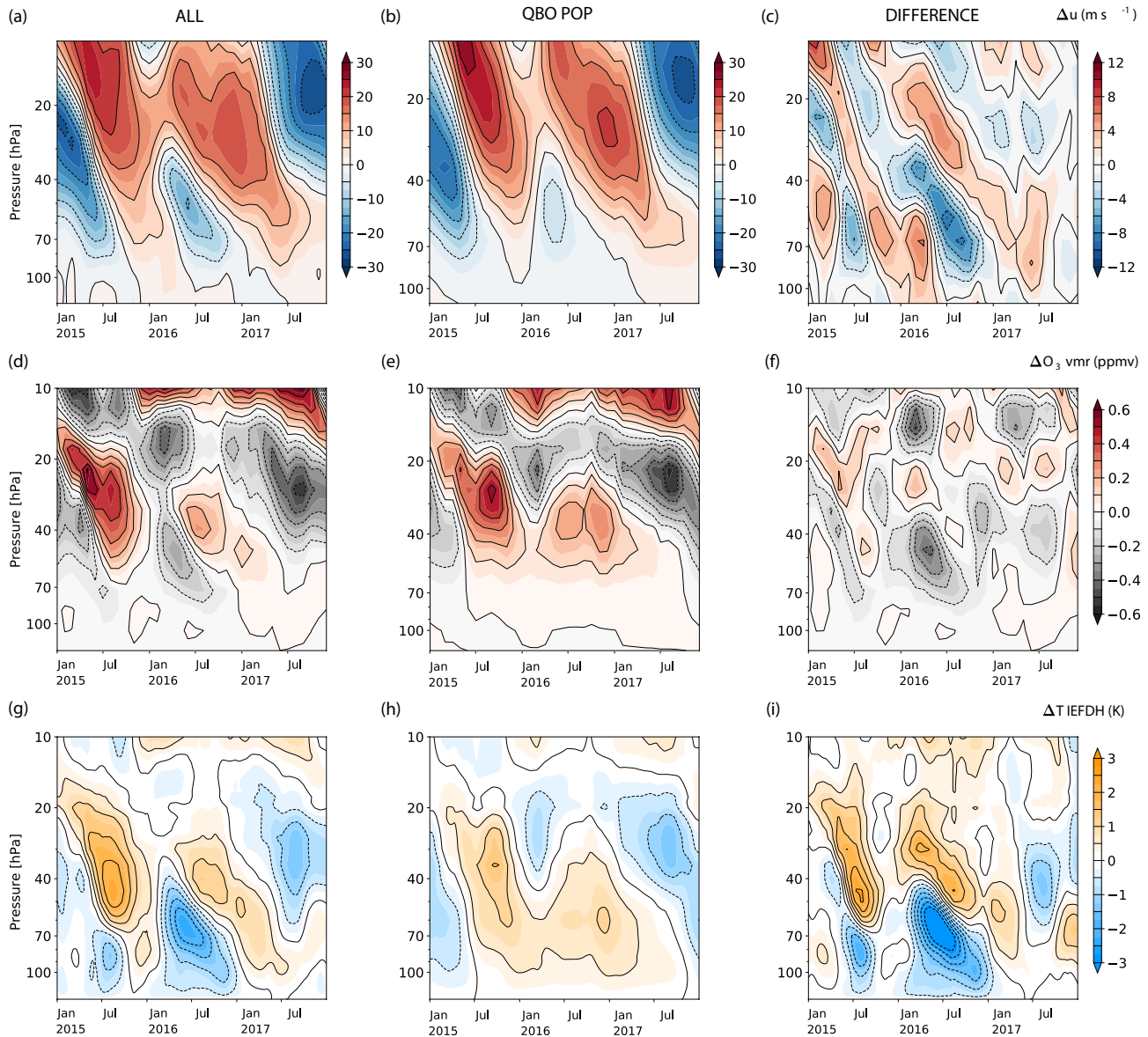


Figure 4. The grid shows the changes in zonal wind (first row), ozone (second row) and temperature from the inter-annually evolving fixed dynamical heating (IEFDH) calculation (third row) during the Quasi-biennial oscillation (QBO) 2016 disruption. All quantities are averaged between 10° N – S. In the first column, the full inter-annual variability (ALL) in zonal wind is shown in (a) and for ozone in (d). The seasonal cycle and trends have been removed. (g) Shows the corresponding IEFDH temperature change from the ozone perturbation in (d). In the second column, the QBO component has been identified as the time series corresponding to the leading Principal Oscillation Pattern (POP) for the zonal wind in (b) and the leading POP in ozone in (e). The corresponding IEFDH temperature change to (e) is shown in (h). The figures (c), (f), and (i) in third column show the difference between corresponding figures from the first column and the second column (ALL minus QBO POP). The second and third rows of figures share the same colorbar.

6. Quantifying the Ozone Radiative Feedback

We have shown that ozone changes are an important contributor to temperature inter-annual variability. We now consider ways to quantify this radiative effect. First it is informative to look at the lagged correlation, calculated at each pressure level, between pairs of ERA5 temperature, dynamical heating and ozone. The Pearson correlation coefficient is shown in Figure 5 and significance is calculated using a non-parametric test which randomizes the phases of the input time series following Ebisuzaki (1997). We include the lagged correlation between ERA5 temperature and water vapor for completeness and will only discuss those briefly since the correlations are low and less important than ozone.

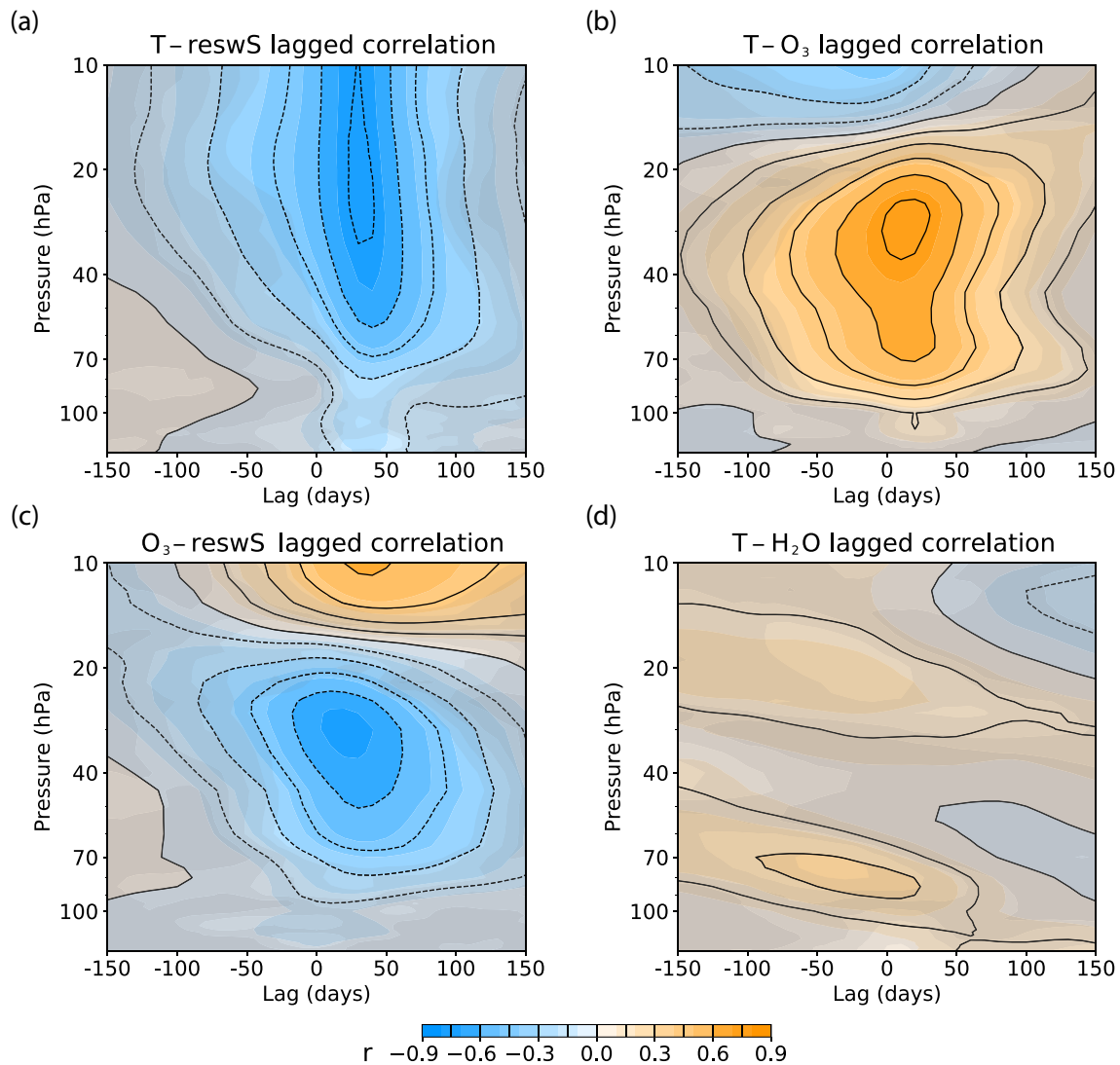


Figure 5. Time (lag) versus height sections created by regressing monthly time series (1995–2019) of (a) temperature versus $\overline{w^* S}$, (b) temperature versus ozone, (c) ozone versus $\overline{w^* S}$ and (d) temperature versus water vapor at different levels and time lags. Positive lags indicate that later values of the first quantity are matched with earlier values of the second quantity. The gray fog which is plotted as overlaid contours with different levels of transparency represents confidence levels of 95%, 90%, 80%, 70%, and 60% using a non-parametric test which randomizes the phases of the input time series following Ebisuzaki (1997).

Figure 5a shows a large negative correlation between temperature and the upwelling term ($-\overline{Q}_{\text{dyn}}$). The correlation is strongest at 20 hPa and decreases lower down toward 70 hPa. At 70 hPa, the correlation peaks around 40 days and decreases to about 30 days at 10 hPa. This is consistent with increased upwelling leading to dynamical cooling and a lagged radiative response in temperature with radiative time scales decreasing with altitude. Ozone is positively correlated with temperature on a broad range of timescales (Figure 5b) with the correlation maximizing at a lag of around 20 days below 20 hPa. Above this region, the photochemistry of ozone becomes important. Below this region, ozone is dynamically controlled. Note that temperatures are more highly correlated with ozone than with the dynamical heating around 70 hPa (Figure 5a). The vertical transport of ozone leads to the structures seen in Figure 5c where an increase in upwelling draws up more ozone poor air, from the troposphere below, into the stratosphere and leads to a decrease in ozone. The largest correlation occurs at 30 hPa at a lag of 20 days. At 70 hPa, these correlations maximize around 40 days. These plots show that as upwelling increases, temperature decreases due to both the dynamical heating change and the ozone decreases as a result of the vertical transport. Hence, there is an important enhancement of the temperature response to the dynamical

heating that comes from the ozone-transport feedback. This can alternatively be thought of as a smaller upwelling being required to maintain a given temperature.

We note that there is an interesting structure in the temperature–water vapor lagged correlation in Figure 5d with a positive lagged correlation starting around the cold point and extending upwards and backwards in lag. Water vapor at the cold point is correlated with temperature at that level and the resulting tape recorder signal in water vapor is advected upwards. Hence the water vapor at any level, and its subsequent temperature effect, is correlated with the water vapor at the cold point (with a lag determined by the speed of the upward transport). Temperatures at different levels are also correlated to each other due to the non-local effects of radiation. These complex non-local interactions lead to the structures seen.

We now quantify the changes in radiative damping rates as follows. The dynamical heating, ozone and water vapor variations form the main contributors to the temperature time series. We will focus on the radiative contribution of ozone and consider the difference between Equation 1 and Equation 2 to give Equation 6. For convenience, we also split the radiative heating into the contribution from ozone changes and those from changes in other trace species (water vapor, aerosol) in Equation 7:

$$\partial_t \Delta \bar{T} - \Delta \bar{Q}_{\text{dyn}} = \bar{Q}_{\text{rad}}(\bar{\chi}, \bar{T}) - \bar{Q}_{\text{rad}}(\bar{\chi}^0, \bar{T}^0), \quad (6)$$

$$= \bar{Q}_{\text{rad}}(\bar{O}_3, \bar{T}) - \bar{Q}_{\text{rad}}(\bar{O}_3^0, \bar{T}^0) + \bar{Q}_{\text{rad}}(\bar{\chi}_{\text{other}}, \bar{T}) - \bar{Q}_{\text{rad}}(\bar{\chi}_{\text{other}}^0, \bar{T}^0), \quad (7)$$

where the radiative heating has been split into a changes due to ozone and changes due to other traces gases excluding ozone ($\bar{\chi}_{\text{other}}$).

The longwave (LW) component of the radiative heating rate change contains a term that arises from the temperature change only, $-\alpha_T \Delta \bar{T}$ (where α_T is a radiative relaxation rate). This allows us to write the right hand side of Equation 6 as

$$\begin{aligned} \partial_t \Delta \bar{T} - \Delta \bar{Q}_{\text{dyn}} &= \bar{Q}_{\text{lw}}(\bar{\chi}^\circ, \bar{T}) - \bar{Q}_{\text{lw}}(\bar{\chi}^\circ, \bar{T}^0) + \Delta \bar{A}_1 \\ &= -\alpha_T \Delta \bar{T} + \Delta \bar{A}_1 \end{aligned} \quad (8)$$

where all other changes in radiative terms, arising from changes in all trace species and from shortwave heating are combined into the term, $\Delta \bar{A}_1$.

Since ozone is correlated with temperature (Figure 5b), we could also split the right hand side of Equation 7 into LW heating terms due to changes in ozone and temperature and changes due to other radiative terms ($\Delta \bar{A}_2$). We also assume that these changes in longwave heating can be written as linear damping term ($-\alpha \Delta \bar{T}$) as in Equation 10.

$$\partial_t \Delta \bar{T} - \Delta \bar{Q}_{\text{dyn}} = \bar{Q}_{\text{lw}}(\bar{O}_3, \bar{T}) - \bar{Q}_{\text{lw}}(\bar{O}_3^0, \bar{T}^0) + \Delta \bar{A}_2 \quad (9)$$

$$= -\alpha \Delta \bar{T} + \Delta \bar{A}_2 \quad (10)$$

We run the radiative code to extract the relevant longwave heating rates when prescribing ERA5 temperature inter-annual variations (\bar{T}). The various damping rates are calculated using linear regression, at every pressure level and latitude, between the heating rates and ERA5 temperatures. The damping timescales, $\tau = 1/\alpha$, and damping rates, α are shown in Figures 6a and 6b respectively and Figure 6c shows the fraction of the variance in longwave heating rates explained by local temperature anomalies. The latitudinal variation in α and the explained variance is shown in Figure S8 of Supporting Information S1.

The solid blue line in Figure 6a shows that the radiative timescale, $1/\alpha_T$, is about 29 days around 70 hPa, increasing to 49 days around 90 hPa. Longwave radiative damping rates are dominated by CO₂ and are dependent on temperature (e.g., Fels, 1982; Hitchcock et al., 2010; Newman & Rosenfield, 1997). Temperature changes explain most of the variance in longwave radiative damping rates ($r^2 > 0.7$ above 70 hPa).

If we including the ozone changes in the longwave heating rates ($1/\alpha$, dashed orange line), as given by Equation 10, the additional correlation between ozone and temperatures leads to a timescale of ~ 55 days at 70 hPa

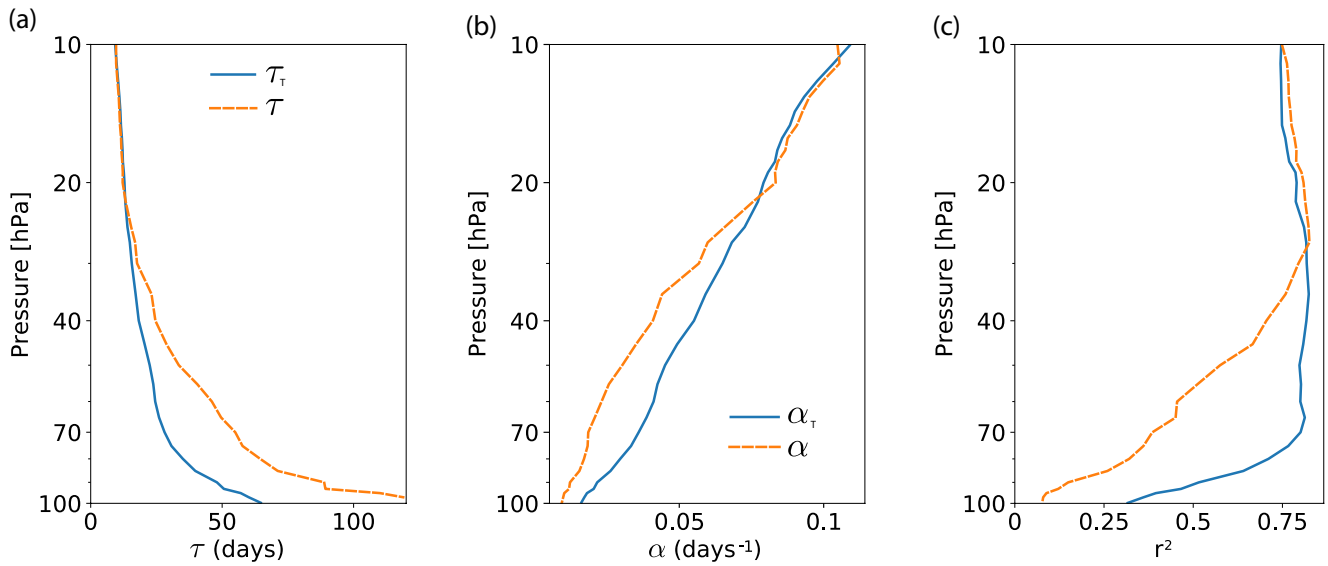


Figure 6. Radiative damping (a) timescales and (b) rates calculated using linear regression of heating rates derived from the radiation code against ERA5 temperatures. The solid blue line shows the regression using longwave heating rate changes from temperature only and the dashed orange line uses longwave heating rate changes from temperature and ozone changes. (c) The fraction of variance in longwave heating rates explained by local temperature anomalies. All values are averaged between 30° N – S.

to ~88 days at 90 hPa (dashed orange line) although the fraction of the variance explained falls rapidly below 40 hPa. These longer timescales are consistent with the value of 70 days obtained by Fueglistaler et al. (2014).

Alternatively, it is more physically relevant to think of the ozone only radiative heating, $\overline{Q}_{\text{rad}}(\overline{O}_3, \overline{T}^\circ) - \overline{Q}_{\text{rad}}(\overline{O}_3^0, \overline{T}^\circ)$, as an enhancement of the dynamical heating since it arises from the transport of ozone by the upwelling. Hence we can also write Equation 6 above as:

$$\begin{aligned} \partial_t \Delta \overline{T} - \Delta \overline{Q}_{\text{dyn}} &= \overline{Q}_{\text{rad}}(\overline{O}_3, \overline{T}^\circ) - \overline{Q}_{\text{rad}}(\overline{O}_3^0, \overline{T}^\circ) - \alpha_T \Delta \overline{T} + \Delta \overline{A}_3 \\ \partial_t \Delta \overline{T} - (1 + \beta) \Delta \overline{Q}_{\text{dyn}} &= -\alpha_T \Delta \overline{T} + \Delta \overline{A}_3 \end{aligned} \quad (11)$$

where β represents the enhancement of the radiative effect of the dynamical heating due to the ozone transport and $\Delta \overline{A}_3$ includes all other radiative terms. Note that we are considering the total change heating rates due to ozone in this case since we argue that upwelling changes ozone and these ozone changes will lead to shortwave and longwave heating. The enhancement in dynamical heating, β , is calculated by linear regression between the ozone only heating rate and the dynamical heating and is shown in Figure 7.

Figure 7a shows that we can think of the ozone-transport effect as enhancing the dynamical heating term as in Equation 11. The increase is substantial and of about 20% at 70 hPa and peaking at 40% at 35 hPa. The additional radiative effect of the vertical transport of ozone translates into a smaller upwelling being required to cause the same temperature change. The quality of the fit is poor for the 30° N – S average, as shown by Figure 7b but improves in the region 10° N – S (see Figure S8 in Supporting Information S1) which could be due to a better correlation between upwelling and ozone within the latitude range where the QBO has a strong influence. We also note that the results in Figure 7a are not consistent with those in Figure 6; values of β are smaller than what would be expected from the changes in α . Ozone is more strongly correlated with temperatures below 40 hPa than with the dynamical heating as seen in Figures 5b and 5c. This could be due to other processes contributing to ozone changes other than upwelling in this region.

7. Discussion

We have shown that it is possible to reproduce the inter-annual variability in lower stratospheric temperatures using a 1D radiative calculation. Such a calculation allows us to decompose the temperature changes into various components. We apply various continuous perturbations and calculate heating rates using a radiative calculation.

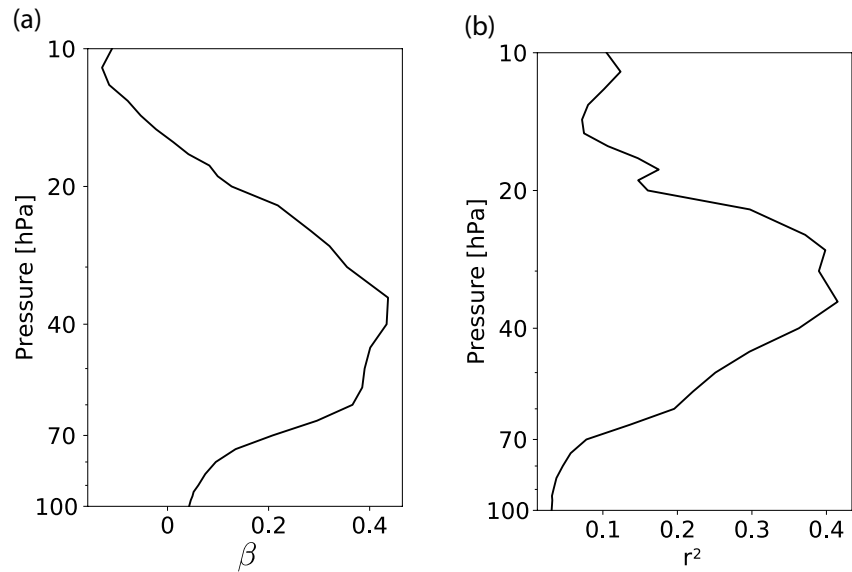


Figure 7. (a) Enhancement of dynamical heating due to ozone-transport radiative feedback calculated using linear regression of heating rate arising from ozone only against the dynamical heating. (b) The fraction of variance in dynamical heating explained the linear regression with ozone only heating rates. All values are averaged between 30° N – S.

The heating rates are then used to update temperature whilst keeping the dynamical heating fixed. This inter-annually evolving fixed dynamical heating calculation (IEFDH) calculation is an extension of a similar calculation used for seasonal cycle changes (Forster et al., 2007). By calculating the temperature change using this new technique, we are able quantify the contribution from ozone, water vapor, aerosol and the linear trend in carbon dioxide. This calculation is further modified, by allowing the dynamical heating to vary, to quantify temperature changes due to the inter-annual variability in upwelling.

The temperature variability in the tropical lower stratosphere is typically well constrained in modern reanalyses compared to upwelling. The fact that the IEFDH calculation is able to reproduce to closely reproduce the temperature variability in the tropics gives confidence to the representation of inter-annual variability in upwelling in ERA5 and of trace gases in SWOOSH. Hence, this calculation also serves as an independent consistency check based on a physical process.

We have shown that at 70 hPa, the ± 3 K inter-annual changes in temperature can primarily be explained by variations in dynamical heating (up to ± 2.1 K) and variations in ozone (up to ± 1.6 K). A smaller contribution (up to ± 0.4 K) arises from water vapor changes. Aerosol changes and the linear trend in carbon dioxide make up most of the remaining variability. The contributions from aerosols dominate the time series during the 1991 Pinatubo volcanic eruption, with changes up to 3.3 K at the peak, a few months after the eruption. Carbon dioxide adds a linear warming of about 0.2 K over the time period from 1984 to 2019.

This calculation emphasizes the substantial role of ozone in contributing to the inter-annual variability in temperature. In the lower stratosphere, the ozone budget is dominated by transport and increases in upwelling act to decrease ozone. This feedback amplifies the temperature response to a change in upwelling. Temperature changes are positively correlated to ozone change and negatively correlated to the upwelling. The transport feedback means that for a given change in upwelling, the additional changes in ozone result in a larger temperature change than would be expected simply from the change in dynamical heating. This can also be thought of as a smaller change in upwelling being required to achieve the same temperature change or as an increase in the radiative damping time scale. We have quantified these changes using the radiative calculation and find including the ozone correlation with temperature changes the radiative damping time scale by 50% at 70 hPa to about 56 days. Instead, if we view the ozone changes as primarily arising from changes in upwelling, this transport effect enhances the dynamical heating term by 20% at 70 hPa and peaking at 40% at 35 hPa. We find that these two approaches do not yield similar results since the ozone-temperature correlation is stronger than the ozone-upwelling correlation.

A component of the ozone variability related to the QBO is extracted using a POP analysis. The time series that corresponds to the leading POP is used to calculate the QBO induced ozone temperature change in the IEFDH calculation. This corresponds to a temperature change of about ± 1 K at 70 hPa. We also find a substantial amount of non-QBO variability, especially in the region below 40 hPa. This is particularly visible around the Pinatubo volcanic eruption, and around the years 2000 and 2011 which coincide with previously reported water vapor drop events.

The POP analysis also allowed us to look in more detail at the unusual QBO disruption in 2016 during which a shallow westward jet formed within the eastward phase of the QBO in the lower stratosphere. Assuming the QBO POP timeseries represents the “regular” QBO, we can obtain the anomalous ozone change during the disruption and calculate the corresponding IEFDH temperature change. If 2016 were a regular QBO year, we would have expected ozone to contribute to warming in the region below 40 hPa. Instead, the ozone change arising from the disruption leads to a dipole structure around 40 hPa with a maximum cooling of 3 K at 70 hPa and a warming above with a maximum of 2 K at 30 hPa. This dipole structure follows the descending wind shear associated with the disruption. Together with the change in temperature from dynamical heating, the QBO 2016 disruption caused a large anomaly in temperature comparable to the Pinatubo volcanic eruption.

The IEFDH calculation also shows that water vapor changes are a secondary contributor to the temperature change (about ± 0.3 K at 70 hPa). The increase in carbon dioxide is assumed to be linear and adds a linear increase of 0.2 K between 1984 and 2019. The smaller volcanic eruptions, after the year 2000, do not have a significant effect on temperatures (less than 0.1 K at the peak).

The IEFDH calculation shows that it is possible to attribute inter-annual changes in temperature to specific factors with reasonable accuracy and opens the possibility of more detailed studies into the feedbacks between dynamics and radiation. Ozone changes are large and enhance dynamical changes via the transport coupling. This effect will not be captured, for instance, by climate models using an ozone climatology. Furthermore, we have shown that the QBO 2016 disruption provides both an interesting case study and a test of the internally generated QBO in climate models. To be able to capture the correct temperature change relies on the model accurately simulating the changes to waves, the accompanying ozone transport changes and the subsequent radiative impact on the dynamics.

Appendix A: Correlation Between IEFDH and ERA5 Temperatures

Figure A1 shows the square of the correlation coefficient, r^2 , between the IEFDH calculation and ERA5 temperature data shown in Figure 1 for the time period 1984–1991 in (a) and 1992–2019 in (b). There is a strong correlation between the time series above 70 hPa and poorer agreement below 70 hPa.

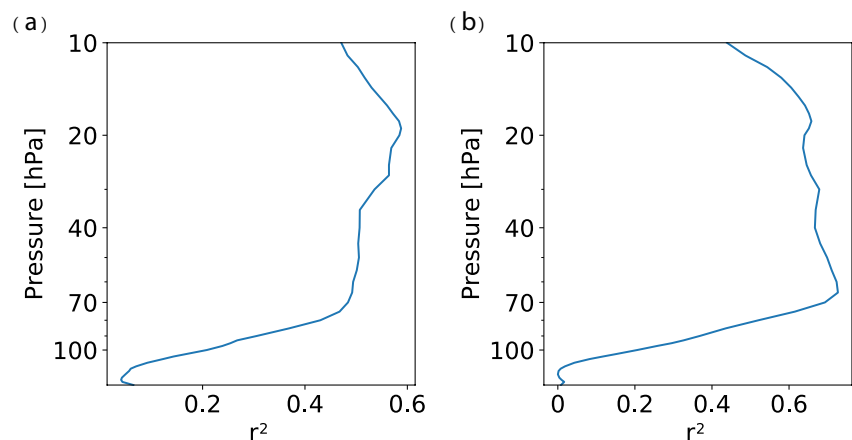


Figure A1. Correlation coefficient, r^2 , at different pressure levels between the 30° N – S average of temperature changes in the inter-annually evolving fixed dynamical heating calculation and in ERA5. The time series is split into two sections: (a) 1984–1991 and (b) 1992–2019.

Appendix B: CO₂ Linear Trend

The vertical profile of temperature change between 2019 and 1984 due to the CO₂ linear trend is shown in Figure B1. CO₂ has been assumed to be well mixed and to be increasing linearly from 345 ppmv (1984 value) to 412 ppmv (2019 value). Carbon dioxide is the dominant emitter in the stratosphere and increasing carbon dioxide leads to increases cooling throughout most of the stratosphere from the increase in longwave emission. In the tropical lower stratospheric region (30 hPa and below), the longwave emission is small and the shortwave heating dominates causing the temperature increase seen. This is only the case over the latitude range where there is high solar insolation: 30° N – S on average and shifting with season. Our results are consistent with those of Wang and Huang (2020) but the vertical extent of the warming is somewhat broader and results in Huang and Wang (2019) suggest that there are temperature biases in the predicted response from different radiation codes.

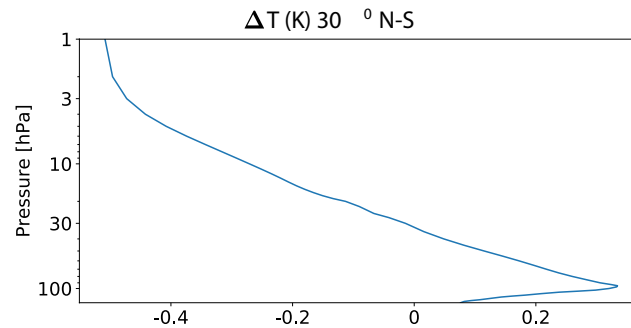


Figure B1. Difference in temperature, calculated from the radiative calculation, between 2019 and 1984 due to the CO₂ linear trend. The values are averaged between 30° N – S.

Appendix C: Principal Oscillation Pattern (POP) Analysis

A brief summary of the Principal Oscillation Pattern (POP) analysis is given below. For detailed descriptions, we refer the reader to (Gallagher et al., 1991; von Storch & Zwiers, 2002; Xu, 1992).

Consider the time evolution of a linear dynamical system, where vectors are in bold lowercase letters and matrices are in bold uppercase letters:

$$\frac{d\mathbf{x}(t)}{dt} = \mathbf{A}\mathbf{x}(t) + \boldsymbol{\xi}(t) \quad (\text{C1})$$

where $\mathbf{x}(t)$ is some quantity of interest, such as the zonal wind, which varies with time t , \mathbf{A} is some constant matrix and $\boldsymbol{\xi}(t)$ is some noise vector.

Discretization of Equation C1 leads to

$$\mathbf{x}(t + 1) = \mathbf{B}\mathbf{x}(t) + \boldsymbol{\xi}(t) \quad (\text{C2})$$

where \mathbf{B} is related to \mathbf{A} and the details of the discretization.

The eigenvectors, \mathbf{p} , of \mathbf{B} are the POPs and there are corresponding eigenvalues, λ . The matrix \mathbf{B} is, in general, not symmetric and some of the eigenvalues may be complex. Since $\mathbf{x}(t)$ and \mathbf{B} are real, any complex eigenvalues and eigenvectors occur in conjugate pairs. In most cases, all the eigenvalues are different and the eigenvectors form a linear basis.

If the dynamics of the system are known, the process matrix, \mathbf{B} , can be obtained analytically but in general, this is not the case. \mathbf{B} can be estimated from the $\mathbf{B} = \mathbf{C}(\tau)\mathbf{C}(0)^{-1}$, where $\mathbf{C}(\tau)$ and $\mathbf{C}(0)$ are the lag- τ and lag-0 covariance matrices obtained from $\mathbf{x}(t)$.

At any time, t , the state $\mathbf{x}(t)$ can be expressed in terms of the eigenvectors of \mathbf{B} as follows

$$\mathbf{x}(t) = \sum_i a_i(t) \mathbf{p}_i \quad (\text{C3})$$

where we are summing over all the POPs and $a_i(t)$ are called the POP coefficients.

From Equation C2 and C3, $a_i(t)$ satisfies

$$a_i(t+1) = \lambda_i a_i(t) + \xi(t) \quad (\text{C4})$$

In the absence of noise, $\xi(t) = 0$, $a_i(t) = \lambda_i^t a_i(0)$. If we express λ_i as $|\lambda_k| \exp(i\omega_i)$, with $|\lambda_k| \leq 1$ (an amplifying and therefore non-physical solution would result from $|\lambda_k| > 1$), we can write

$$a_i(t) = \exp\left(-\frac{t}{\tau_i}\right) \exp\left(i \frac{2\pi t}{T_i}\right) a_i(0) \quad (\text{C5})$$

with an e-folding (decay) time of $\tau_i = -1/\log |\lambda_k| > 0$ and an oscillation period, $T_i = 2\pi/\omega_i$.

The time series of POP coefficients, $a(t)$ can be computed for each POP, \mathbf{p} , as follows:

$$a(t) = \mathbf{x}(t) \cdot \mathbf{q} \quad (\text{C6})$$

where \mathbf{q} is the corresponding Principal Adjoint Pattern. \mathbf{q} are the eigenvectors of the transposed matrix, \mathbf{B}^T .

Finally, we can interpret n of the POPs (usually one or two) as modeling the original time series. Consider a predictor, $\rho(t)$, which is attempting to model the predictand, $\mathbf{x}(t)$, with some error in the prediction, $\mathbf{r}(t)$, such that $\mathbf{x}(t) = \rho(t) + \mathbf{r}(t)$. $\rho(t)$ is given by

$$\rho(t) = \sum_n a_k(t) \mathbf{p}_k \quad (\text{C7})$$

where the sum is taken over a subset, n , of the relevant POPs. This quantity is what we refer to as the time series associated with a certain relevant POP in the main text (for example, the time series associated to the leading QBO ozone POP in Section 5).

In the case of the QBO, we extract the QBO-related variability in zonal mean zonal wind and zonal mean ozone using a POP analysis. We use data between 20° N – S and 10 to 1,000 hPa. The seasonal cycle and linear trends are removed before the analysis. For computational efficiency, the process is done in empirical orthogonal function (EOF) space and we do not truncate the EOFs. To estimate the matrix, B , we need to calculate lag covariances and choose a lag of 9 months for the zonal wind and 12 months for ozone. Vertical pressure weighting, as used in Sheshadri and Plumb (2017) does not substantially affect this calculation and we do not weight the fields. Using the various methods in Gallagher et al. (1991), we check that leading POP obtained is sensible. Choosing a different lag, provided it is long enough, will yield a slightly different leading POP but with very similar spatial patterns. We tested lags between 9 and 14 months and simply choose the lag where the leading POP explained most of the variance. For the zonal wind, the real and imaginary parts of the leading POP, which explains 47% of the variance, is shown in Figures C1a and C1b. These are very similar to the leading EOFs (Figures C1c and C1d) which adds confidence to the analysis. The leading POP has a decay timescale of 71.8 months and an oscillation timescale of 28.2 months. For ozone, leading POP (explaining 30% of the variance) has a decay timescale of 97.9 months and an oscillation timescale of 27.6 months.

We also construct the zonal wind and the ozone timeseries that corresponds to the leading QBO POPs according to Equation C7.

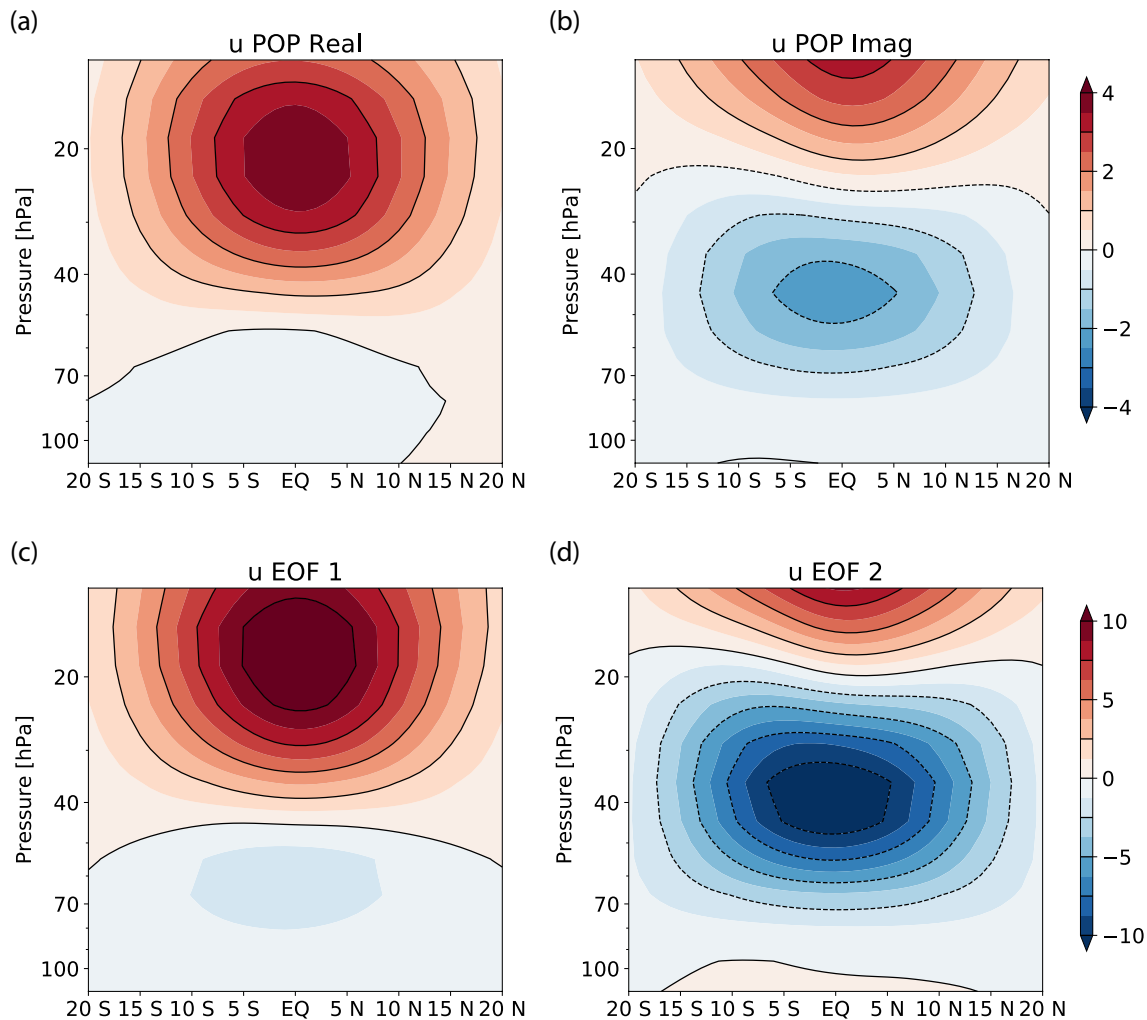


Figure C1. (a) Real and (b) imaginary components of the leading Principal Oscillation Pattern calculated from the deseasonalized and detrended ERA5 zonal mean zonal wind. (c) First and (d) second Empirical Orthogonal functions for comparison. Rows of plots share the same colorbars.

Data Availability Statement

SWOOSH data can be downloaded from <https://csl.noaa.gov/groups/csl8/swoosh/>. The ERA and ERA5.1 datasets were obtained from the Copernicus Climate Change Service at <https://cds.climate.copernicus.eu/>. The GLOSSAC V2.0 data were obtained from https://asdc.larc.nasa.gov/project/GloSSAC/GloSSAC_2.0.

Acknowledgments

A. Ming would like to acknowledge support from the Leverhulme Trust and the Newton Trust as an Early Career Fellow. The authors thank Aditi Sheshadri, Alan Plumb, Anja Schmidt, and Peter Haynes for discussions on various aspects of this work. The authors also thank Stephan Fueglistaler and two anonymous reviewers that provided detailed comments and raised interesting discussion points that greatly improved this manuscript. The authors would also like to acknowledge the useful discussions with William Randel that helped our understanding of the lower stratosphere.

References

- Andrews, D. G., Holton, J. R., & Leovy, C. B. (1987). *Middle atmosphere dynamics*. Academic Press.
- Avery, M., Davis, S., Rosenlof, K., Ye, H., & Dessler, A. (2017). Large anomalies in lower stratospheric water vapour and ice during the 2015–2016 El Niño. *Nature Geoscience*, *10*, 405–409. <https://doi.org/10.1038/ngeo2961>
- Brinkop, S., Dameris, M., Jöckel, P., Garny, H., Lossow, S., & Stiller, G. (2016). The millennium water vapour drop in chemistry–climate model simulations. *Atmospheric Chemistry and Physics*, *16*(13), 8125–8140. <https://doi.org/10.5194/acp-16-8125-2016>
- C3S. (2017). *ERA5: Fifth generation of ECMWF atmospheric reanalyses of the global climate copernicus climate change Service climate data store (CDS)*. <https://doi.org/10.5065/D6X34W69>
- Chae, J. H., & Sherwood, S. C. (2007). Annual temperature cycle of the tropical tropopause: A simple model study. *Journal of Geophysical Research*, *112*(D19), D19111. <https://doi.org/10.1029/2006JD007956>
- Charlesworth, E. J., Birner, T., & Albers, J. R. (2019). Ozone transport-radiation feedbacks in the tropical tropopause layer. *Geophysical Research Letters*, *46*(23), 14195–14202. <https://doi.org/10.1029/2019GL084679>
- Davis, S. M., Rosenlof, K. H., Hassler, B., Hurst, D. F., Read, W. G., Vömel, H., & Damadeo, R. (2016). The stratospheric water and ozone satellite homogenized (SWOOSH) database: A long-term database for climate studies. *Earth System Science Data*, *8*(2), 461–490. <https://doi.org/10.5194/essd-8-461-2016>

- Dhomse, S., Weber, M., & Burrows, J. (2008). The relationship between tropospheric wave forcing and tropical lower stratospheric water vapor. *Atmospheric Chemistry and Physics*, 8(3), 471–480. <https://doi.org/10.5194/acp-8-471-2008>
- Diallo, M., Riese, M., Birner, T., Konopka, P., Müller, R., Hegglin, M. I., & Ploeger, F. (2018). Response of stratospheric water vapor and ozone to the unusual timing of El Niño and the QBO disruption in 2015–2016. *Atmospheric Chemistry and Physics*, 18(17), 13055–13073. <https://doi.org/10.5194/acp-18-13055-2018>
- Ebisuzaki, W. (1997). A method to estimate the statistical significance of a correlation when the data are serially correlated. *Journal of Climate*, 10(9), 2147–2153. [https://doi.org/10.1175/1520-0442\(1997\)010<2147:AMTETS>2.0.CO;2](https://doi.org/10.1175/1520-0442(1997)010<2147:AMTETS>2.0.CO;2)
- Fels, S. (1982). A parameterization of scale-dependent radiative damping rates in the middle atmosphere. *Journal of the Atmospheric Science*, 39, 11412–1152. [https://doi.org/10.1175/1520-0469\(1982\)039<1141:APOSDR>2.0.CO;2](https://doi.org/10.1175/1520-0469(1982)039<1141:APOSDR>2.0.CO;2)
- Forster, P. M., Bodeker, G., Schofield, R., Solomon, S., & Thompson, D. (2007). Effects of ozone cooling in the tropical lower stratosphere and upper troposphere. *Geophysical Research Letters*, 34(23), 1–5. <https://doi.org/10.1029/2007GL031994>
- Forster, P. M. F., Freckleton, R. S., & Shine, K. P. (1997). On aspects of the concept of radiative forcing. *Climate Dynamics*, 13(7–8), 547–560. <https://doi.org/10.1007/s003820050182>
- Fueglistaler, S., Abalos, M., Flannaghan, T. J., Lin, P., & Rande, W. J. (2014). Variability and trends in dynamical forcing of tropical lower stratospheric temperatures. *Atmospheric Chemistry and Physics*, 14(24), 13439–13453. <https://doi.org/10.5194/acp-14-13439-2014>
- Fueglistaler, S., Haynes, P. H., & Forster, P. M. (2011). The annual cycle in lower stratospheric temperatures revisited. *Atmospheric Chemistry and Physics*, 11(8), 3701–3711. <https://doi.org/10.5194/acp-11-3701-2011>
- Fueglistaler, S., Liu, Y., Flannaghan, T., Haynes, P., Dee, D., Read, W., & Bernath, P. (2013). The relation between atmospheric humidity and temperature trends for stratospheric water. *Journal of Geophysical Research: Atmospheres*, 118(2), 1052–1074. <https://doi.org/10.1002/jgrd.50157>
- Gallagher, F., von Storch, H., Schnur, R., & Hanneschöck, G. (1991). *The POP manual* (Technical Report). Deutsches Klimarechenzentrum. https://doi.org/10.2312/WDCC/DKRZ_Report_No01
- Garfinkel, C. I., Gordon, A., Oman, L. D., Li, F., Davis, S., & Pawson, S. (2018). Nonlinear response of tropical lower-stratospheric temperature and water vapor to ENSO. *Atmospheric Chemistry and Physics*, 18(7), 4597–4615. <https://doi.org/10.5194/acp-18-4597-2018>
- Gilford, D., & Solomon, S. (2017). Radiative effects of stratospheric seasonal cycles in the tropical upper troposphere and lower stratosphere. *Journal of Climate*, 30(8), 2769–2783. <https://doi.org/10.1175/JCLI-D-16-0633.1>
- Gilford, D., Solomon, S., & Portmann, R. (2016). Radiative impacts of the 2011 abrupt drops in water vapor and ozone in the tropical tropopause layer. *Journal of Climate*, 29, 151029140234000. <https://doi.org/10.1175/JCLI-D-15-0167.1>
- Hersbach, H., Bell, B., Berrisford, P., Hirahara, S., Horányi, A., Muñoz-Sabater, J., & Thépaut, J.-N. (2020). The ERA5 global reanalysis. *Quarterly Journal of the Royal Meteorological Society*, 146(730), 1999–2049. <https://doi.org/10.1002/qj.3803>
- Hitchcock, P., Shepherd, T. G., & Yoden, S. (2010). On the approximation of local and linear radiative damping in the middle atmosphere. *Journal of the Atmospheric Sciences*, 67(6), 2070–2085. <https://doi.org/10.1175/2009JAS3286.1>
- Huang, Y., & Wang, Y. (2019). How does radiation code accuracy matter? *Journal of Geophysical Research: Atmospheres*, 124(20), 10742–10752. <https://doi.org/10.1029/2019JD030296>
- Kilian, M., Brinkop, S., & Jöckel, P. (2020). Impact of the eruption of Mt Pinatubo on the chemical composition of the stratosphere. *Atmospheric Chemistry and Physics*, 20(20), 11697–11715. <https://doi.org/10.5194/acp-20-11697-2020>
- Kovilakam, M., Thomason, L. W., Ernest, N., Rieger, L., Bourassa, A., & Millán, L. (2020). The global space-based stratospheric aerosol climatology (version 2.0): 1979–2018. *Earth System Science Data*, 12(4), 2607–2634. <https://doi.org/10.5194/essd-12-2607-2020>
- Li, D., Shine, K. P., & Gray, L. J. (1995). The role of ozone-induced diabatic heating anomalies in the quasi-biennial oscillation. *Quarterly Journal of the Royal Meteorological Society*, 121(524), 937–943. <https://doi.org/10.1002/qj.49712152411>
- Match, A., & Fueglistaler, S. (2021). Anomalous dynamics of QBO disruptions explained by 1D theory with external triggering. *Journal of the Atmospheric Sciences*, 78(2), 373–383. <https://doi.org/10.1175/JAS-D-20-0172.1>
- Maycock, A. C., Joshi, M. M., Shine, K. P., Davis, S. M., & Rosenlof, K. H. (2014). The potential impact of changes in lower stratospheric water vapour on stratospheric temperatures over the past 30 years. *Quarterly Journal of the Royal Meteorological Society*, 140(684), 2176–2185. <https://doi.org/10.1002/qj.2287>
- Ming, A., Maycock, A. C., Hitchcock, P., & Haynes, P. (2017). The radiative role of ozone and water vapour in the annual temperature cycle in the tropical tropopause layer. *Atmospheric Chemistry and Physics*, 17(9), 5677–5701. <https://doi.org/10.5194/acp-17-5677-2017>
- Ming, A., Winton, V. H. L., Keeble, J., Abraham, N. L., Dalvi, M. C., Griffiths, P., & Yang, X. (2020). Stratospheric ozone changes from explosive tropical volcanoes: Modeling and ice core constraints. *Journal of Geophysical Research: Atmospheres*, 125(11), e2019JD032290. <https://doi.org/10.1029/2019JD032290>
- Morcrette, J.-J. (1991). Radiation and cloud radiative properties in the European centre for medium range weather forecasts forecasting system. *Journal of Geophysical Research: Atmospheres*, 96(D5), 9121–9132. <https://doi.org/10.1029/89JD01597>
- Mote, P. W., Holton, J. R., & Boville, B. A. (1994). Characteristics of stratosphere-troposphere exchange in a general circulation model. *Journal of Geophysical Research: Atmospheres*, 99(D8), 16815–16829. <https://doi.org/10.1029/94JD00913>
- Nagashima, T., Takahashi, M., & Hasebe, F. (1998). The first simulation of an ozone qbo in a general circulation model. *Geophysical Research Letters*, 25(16), 3131–3134. <https://doi.org/10.1029/98GL02213>
- NASA/LARC/SD/ASDC. (2018). *Global space-based stratospheric aerosol climatology version 2.0*. NASA Langley Atmospheric Science Data Center DAAC. <https://doi.org/10.5067/GLOSSAC-L3-V2.0>
- Newman, P. A., & Rosenfield, J. E. (1997). Stratospheric thermal damping times. *Geophysical Research Letters*, 24(4), 433–436. <https://doi.org/10.1029/96GL03720>
- Osprey, S. M., Butchart, N., Knight, J. R., Scaife, A. A., Hamilton, K., Anstey, J. A., & Zhang, C. (2016). An unexpected disruption of the atmospheric quasi-biennial oscillation. *Science*, 353(6306), 1424–1427. <https://doi.org/10.1126/science.aah4156>
- Pahlavan, H. A., Fu, Q., Wallace, J. M., & Kiladis, G. N. (2021). Revisiting the quasi-biennial oscillation as seen in ERA5. Part I: Description and momentum budget. *Journal of the Atmospheric Sciences*, 78(3), 673–691. <https://doi.org/10.1175/JAS-D-20-0248.1>
- Plumb, R. A., & Bell, R. C. (1982). A model of the quasi-biennial oscillation on an equatorial beta-plane. *Quarterly Journal of the Royal Meteorological Society*, 108(456), 335–352. <https://doi.org/10.1002/qj.49710845604>
- Poberaj, C. S., Staehelin, J., & Brunner, D. (2011). Missing stratospheric ozone decrease at southern hemisphere middle latitudes after Mt. Pinatubo: A dynamical perspective. *Journal of the Atmospheric Sciences*, 68(9), 1922–1945. <https://doi.org/10.1175/JAS-D-10-05004.1>
- Randel, W. J., Park, M., Wu, F., & Livesey, N. (2007). A large annual cycle in ozone above the tropical tropopause linked to the Brewer-dobson circulation. *Journal of the Atmospheric Sciences*, 64(12), 4479–4488. <https://doi.org/10.1175/2007JAS2409.1>
- Randel, W. J., Wu, F., Vömel, H., Nedoluha, G. E., & Forster, P. (2006). Decreases in stratospheric water vapor after 2001: Links to changes in the tropical tropopause and the Brewer-Dobson circulation. *Journal of Geophysical Research*, 111(D12), D12312. <https://doi.org/10.1029/2005JD006744>

- Robock, A. (2000). Volcanic eruptions and climate. *Reviews of Geophysics*, 38(2), 191–219. <https://doi.org/10.1029/1998RG000054>
- Schoeberl, M. R., Jensen, E. J., Pfister, L., Ueyama, R., Avery, M., & Dessler, A. E. (2018). Convective hydration of the upper troposphere and lower stratosphere. *Journal of Geophysical Research: Atmospheres*, 123(9), 4583–4593. <https://doi.org/10.1029/2018JD028286>
- Sheshadri, A., & Plumb, R. A. (2017). Propagating annular modes: Empirical orthogonal functions, principal oscillation patterns, and time scales. *Journal of the Atmospheric Sciences*, 74(5), 1345–1361. <https://doi.org/10.1175/JAS-D-16-0291.1>
- Stenchikov, G. L., Kirchner, I., Robock, A., Graf, H.-F., Antuña, J. C., Grainger, R. G., & Thomason, L. (1998). Radiative forcing from the 1991 mount pinatubo volcanic eruption. *Journal of Geophysical Research*, 103(D12), 13837–13857. <https://doi.org/10.1029/98JD00693>
- Tegtmeier, S., Anstey, J., Davis, S., Dragani, R., Harada, Y., Ivanciu, I., & Wright, J. S. (2020). Temperature and tropopause characteristics from reanalyses data in the tropical tropopause layer. *Atmospheric Chemistry and Physics*, 20(2), 753–770. <https://doi.org/10.5194/acp-20-753-2020>
- Thuburn, J., & Craig, G. C. (2002). On the temperature structure of the tropical stratosphere. *Journal of Geophysical Research*, 107(D2). <https://doi.org/10.1029/2001jd000448>
- Tummon, F., Hassler, B., Harris, N. R. P., Staehelin, J., Steinbrecht, W., Anderson, J., & Wild, J. (2015). Intercomparison of vertically resolved merged satellite ozone data sets: Interannual variability and long-term trends. *Atmospheric Chemistry and Physics*, 15(6), 3021–3043. <https://doi.org/10.5194/acp-15-3021-2015>
- Tweedy, O. V., Kramarova, N. A., Strahan, S. E., Newman, P. A., Coy, L., Randel, W. J., & Frith, S. M. (2017). Response of trace gases to the disrupted 2015–2016 quasi-biennial oscillation. *Atmospheric Chemistry and Physics*, 17(11), 6813–6823. <https://doi.org/10.5194/acp-17-6813-2017>
- Urban, J., Lossow, S., Stiller, G., & Read, W. (2014). Another drop in water vapor. *Eos, Transactions American Geophysical Union*, 95. <https://doi.org/10.1002/2014EO270001>
- Vernier, J.-P., Thomason, L. W., Pommereau, J.-P., Bourassa, A., Pelon, J., Garnier, A., & Vargas, F. (2011). Major influence of tropical volcanic eruptions on the stratospheric aerosol layer during the last decade. *Geophysical Research Letters*, 38(12), L12807. <https://doi.org/10.1029/2011GL047563>
- von Storch, H., & Zwiers, F. (2002). *Statistical analysis in climate research*. Cambridge University Press. <https://doi.org/10.1017/CBO9780511612336>
- Wang, Y., & Huang, Y. (2020). Understanding the atmospheric temperature adjustment to CO₂ perturbation at the process level. *Journal of Climate*, 33(3), 787–803. <https://doi.org/10.1175/JCLI-D-19-0032.1>
- Xu, J.-S. (1992). On the relationship between the stratospheric quasi-biennial oscillation and the tropospheric southern oscillation. *Journal of the Atmospheric Sciences*, 49(9), 7252–734. [https://doi.org/10.1175/1520-0469\(1992\)049<0725:OTRBTBS>2.0.CO;2](https://doi.org/10.1175/1520-0469(1992)049<0725:OTRBTBS>2.0.CO;2)
- Zhong, W., & Haigh, J. D. (1995). Improved broadband emissivity parameterization for water vapor cooling rate calculations. *Journal of the Atmospheric Sciences*, 52(1), 1242–138. [https://doi.org/10.1175/1520-0469\(1995\)052<0124:IBEPFW>2.0.CO;2](https://doi.org/10.1175/1520-0469(1995)052<0124:IBEPFW>2.0.CO;2)